International Journal of Mechanical Sciences 161–162 (2019) 105060

Contents lists available at ScienceDirect

International Journal of Mechanical Sciences

journal homepage: www.elsevier.com/locate/ijmecsci

Discrete element simulation of surface mechanical attrition treatment with rough-surface sonotrode

Yongmei Zhang[a], Gwénaëlle Proust[a], Delphine Retraint[b], Huamiao Wang[c], Yixiang Gan[a,*]

[a] School of Civil Engineering, The University of Sydney, Sydney, NSW 2006, Australia
[b] ICD-LASMIS, Université de Technologie de Troyes (UTT), CNRS FRE 2019, 12 Rue Marie Curie, 10010 Troyes, France
[c] State Key Laboratory of Mechanical System and Vibration, School of Mechanical Engineering, Shanghai Jiaotong University, Shanghai 200240, China

ARTICLE INFO

Keywords:
SMAT
Discrete element method
Surface treatment
Surface roughness

ABSTRACT

Surface mechanical attrition treatment (SMAT) is a specialized cold working method that is used to induce compressive residual stresses and refine crystalline grains at the surface of metal components. This technique is increasingly employed in different industries, and the control and optimization of the method require fundamental understanding and accurate process modelling, in particularly detailed information regarding the shot-target interaction. This paper presents a Discrete Element Method (DEM) study of the shot dynamics with rough sonotrodes. These rough surfaces are created by grouping in a hexagonal packing of identical spheres. Different roughness values are obtained by varying the sphere diameter and spacing. The coefficient of restitution (CoR) between shot and target used in our DEM simulations was obtained from Finite Element Method (FEM) simulations of multiple shot-target impacts. The DEM results are analyzed after the SMAT process has reached the steady state. The relationships between surface roughness and the resulting impact angle and velocity distributions are investigated. Furthermore, based on a parametric study, we conducted correlation analyses between processing parameters and shot dynamics, and identified key conditions, using the mechanistic models. The proposed numerical method and findings of this study could be used to tailor the SMAT processes.

1. Introduction

Material properties related to surface properties and structure, such as fatigue, wear resistance, bio-compatibility and corrosion resistance, determine the applicability and serviceability of materials [1–4]. Surface treatments have become a major step towards recent developments of metallic materials to increase their performance [5–8], e.g., improved lifetime as most failure initiates on the surface of these components or increase wear resistance. Surface mechanical attrition treatment (SMAT) [9–12], a simple, yet flexible and cost-effective method, has been widely used to improve mechanical properties of metals, such as 316 L stainless steel, which is a widely used alloy for biomedical applications [13–16]. This process generates a nanocrystalline layer at the surface of the treated material [17–20], which, due to the large fraction of grain boundaries and compressive residual stresses, presents extraordinary strength, fatigue life and wear resistance [21–25]. During SMAT, a sonotrode generates ultrasonic vibrations, propelling shot particles inside the enclosed chamber to impact the surface of the target. Due to the high vibration frequency, the target surface is impacted by the shot at high speed over a short duration, causing the surface to undergo severe plastic deformation [26, 27]. So far, the mechanisms for nanocrystalline generation during SMAT and the properties of SMATed material have been well researched; however, how to control the process to achieve specific microstructure and material properties is yet to be fully understood.

Existing experiments showed that the processing parameters, including the vibration amplitude and frequency of the sonotrode, number and size of the shot, geometrical features of the chamber, and treatment duration, determine the resulting microstructure, surface topography and mechanical properties of the treated materials. Liu et al. [10] demonstrated that the treatment duration did not affect the grain size in the top layer, but increased the nanostructured layer thickness of 316 L stainless steel. Li et al. [28] concluded that treatment duration increased the thickness of the deformed layer, but had no influence on the microhardness and surface roughness of pure Mg and Mg-1Ca alloy. Arifvianto et al. showed that shot diameters affected the surface roughness and resulting surface energy of AISI 316 L stainless steel [29]. The surface roughness decreased with treatment duration during the first several minutes and then reached a constant value on the primarily rough target [30,31]. The increasing number and diameter of shot, and the vibration frequency of the sonotrode increased the surface microhardness [32]. Sun et al. [33] presented different fatigue properties of 316 L

* Corresponding author.
E-mail address: yixiang.gan@sydney.edu.au (Y. Gan).

https://doi.org/10.1016/j.ijmecsci.2019.105060
Received 7 June 2019; Received in revised form 19 July 2019; Accepted 1 August 2019
Available online 2 August 2019
0020-7403/

stainless steel with two different SMAT conditions: high and very high, achieved by adjusting the treatment duration and vibration frequency of the sonotrode. All these studies mostly analyzed the different surface properties obtained while varying just one or two processing parameters, but none investigated the role of all the processing parameters at once limiting the optimization of the process itself. One exception to this limitation can be found in the studies realized by Zhu et al. [34, 35] where the effects of treatment duration, shot diameter, sonotrode vibration amplitude, and chamber height on surface roughness, hardness and hydrophilicity of pure titanium were investigated. Through fitting the experimental data, they proposed empirical equations describing relationships between processing parameters and surface roughness and hardness. However, since these relationships were obtained using only certain processing cases they cannot be straightforwardly generalized. Unfortunately, realizing an entire set of experiments where all the processing parameters would vary over a large range of values would be both time consuming and costly.

The microstructure, surface topography and mechanical properties of treated materials depend on the severe plastic deformation history during SMAT [27]. Some researchers attempted to investigate the resulting strain state using a theoretical approach. Huang et al. [36] built an analytical model related to the total energy of the system to estimate the correlation between processing parameters and the resulting shot velocity, strain rate deformation and obtained grain size. This particular approach ignored shot-shot and shot-chamber collision, and the velocity of shot was taken as an average value. Chaise et al. [37] calculated the average plastic strain tensor using semi-analytical method and then transferred it into finite element method (FEM) to predict the deformation and residual stresses. In this model, the impact positions and velocities were imposed. FEM can also be directly used for predicting the distribution of residual stresses, work- hardening and surface roughness. Zhang et al. [38] conducted single shot impact simulation to calculate the indent size with varying shot diameter and impact angle. Multiple shot particles simulation was carried out to determine the residual stress and vertical displacement at the surface of the target. Dai et al. [39] identified the surface roughening mechanism related to treatment duration by means of FEM and found that a smaller shot size leads to a lower surface roughness and a thinner strengthened layer. These FEM and analytical models need shot-target impacts as input parameters, like impact velocities, impact angles and spatial impact distribution of shot. With the detailed and accurate knowledge of the realistic shot impact information, one can calculate the strain state at different depth by theoretical analysis or numerical modelling. By employing high-speed cameras, Chan et al. [27] measured the impact velocities of multiple shot particles and Badreddine [38] and Dai et al. [39] observed the shot trajectories inside the chamber. Due to the difficulty of capturing the exact moment of shot-target collision, the data obtained from experiments are limited.

Discrete element method (DEM), which handles complex and random interactions of particles, can be used to investigate the effects of the process parameters on the resulting impact locations, impact velocities and impact angles. Badreddine et al. proposed a numerical model to predict the shot dynamics and studied the influence of chamber shape [40], shot diameter and number, and vibration amplitude of the sonotrode [41] on the induced impact distribution. In their simulations, a smooth sonotrode was utilized and small initial velocities with random directions were assigned to the shot to ensure numerical efficiency. The simulated impact angles were almost 90° to the target surface and the distribution of impact velocity showed a binary distribution, which are in contradiction with the experimental observations [42]. In reality, the perfectly smooth surface of the sonotrode causes, after a few impacts for a given shot, a perfectly vertical motion of the shot even if initially a specific direction was assigned to each shot. Using a rough-surface sonotrode will produce random impact directions for all shot particles during the entire duration of the simulation. Surface coverage and compressive residual stress distribution can thus be spatially uniform due to the multidirectional shot impacts, which replicates one of the advantages of SMAT over traditional shot peening.

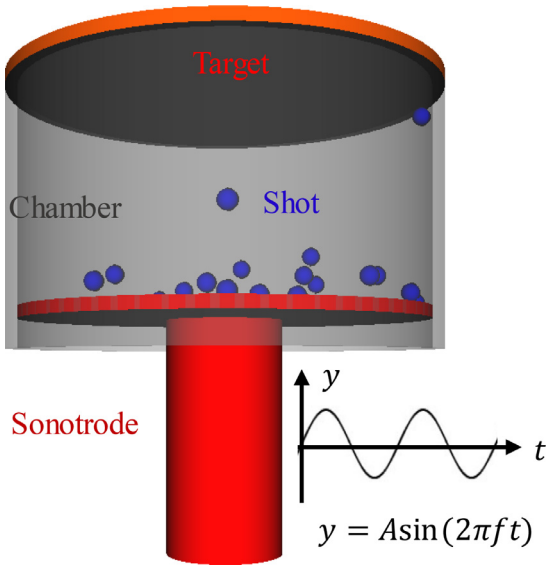

Fig. 1. Schematics of a typical SMAT setup.

In this study, we propose a numerical model to simulate the SMAT process with a rough-surface sonotrode and to investigate the effects of the different processing parameters on shot-target interactions. The rough surface of the sonotrode is created by grouping identical spheres in a hexagonal pattern. Simulations of multiple shot-target impacts are conducted by FEM to obtain the indent size and coefficient of restitution (CoR) between shot and target. The Avrami model describing coverage evolution with treatment duration is provided with good agreement with DEM simulation result. The steady state regime of the SMAT process is examined to ensure the validity of the analysis. The results of the DEM simulations are recorded in term of shot impact number, impact velocity and impact angle distribution. The effects of the sonotrode roughness on the distributions of impact angle and vertical velocity are carefully investigated. Thereafter, the effects of the processing parameters, including the vibration amplitude and frequency of the sonotrode, the number and size of shot, the height of the chamber, and the treatment duration are also studied.

2. Numerical modelling

2.1. Discrete element model

The SMAT setup used in these simulations is illustrated in Fig. 1. In order to simulate shot dynamics in the enclosed cylindrical chamber, a three-dimensional DEM model was created using the open-source particle simulation software LIGGGHTS. Shot particles are modelled as elastic isotropic spherical bodies here. Particle-wall (including sonotrode, chamber, and target) interaction can be calculated by treating the walls as finite polygon surfaces. The motion of each wall can be prescribed, such as rotating and vibrating.

The Hertzian tangential history model is selected from the existing framework to analyze the shot-shot, shot-target and shot-chamber interactions. In the normal direction of contact, the analytical solution for the contact force is given by Hertzian law. According to the law, the normal force (F_n) has two terms, a spring force and a damping force with a non-linear relationship

$$F_n = F_n^s - F_n^d \ . \tag{1}$$

Considering the contact between two particles (e.g., ith and jth particles) with elastic moduli E_i and E_j, Poisson's ratios ν_i and ν_j, and radii

Table 1
The geometry and process parameters (see Fig. 2(c)).

Geometry	Inner radius of chamber [45] (mm)	35
	Radius of target (mm)	37
	Height of the chamber (target-to-sonotrode) [40] (mm)	20, 30, 34, 38, 60
Process	Frequency of vibration of the sonotrode [40,44] (kHz)	10, 20
	Amplitude of vibration of the sonotrode [40,43] (μm)	10, 25, 50
	Shot diameter [41] (mm)	3, 4, 5
	Shot number [42]	50, 100, 150
	Coefficients of friction between components [46]	0.05
	Timestep (s)	1.5×10^{-7}

Table 2
Material parameters used in all the simulation cases [47–50].

	Shot	Sonotrode	Chamber	Target
Material	AISI 304 [49]	Ti6Al4V [50]	Hardened steel [48]	AISI 316 L [47]
Density (kg/m^3)	7900	4429	7850	7908
Young's modulus (GPa)	200	110	205	210.3
Poisson's ratio	0.29	0.31	0.29	0.27

R_i and R_j, respectively, the spring force is defined as a function of the normal overlap distance of two particles δ_n

$$F_n^s = \frac{4}{3}E^*\sqrt{R^*}\delta_n^{\frac{3}{2}}, \tag{2}$$

where the equivalent elastic modulus E^* and the equivalent radius R^* are defined by

$$\frac{1}{E^*} = \frac{1-\nu_i^2}{E_i} + \frac{1-\nu_j^2}{E_j} \tag{3}$$

$$\frac{1}{R^*} = \frac{1}{R_i} + \frac{1}{R_j}\,. \tag{4}$$

On the other hand, the damping force F_n^d is given by

$$F_n^d = -2\sqrt{\frac{5}{6}}\beta\sqrt{S_n m^*}\,\upsilon_n \tag{5}$$

where v_n is the normal component of the relative velocity between two particles. The parameter β, the normal stiffness S_n, and the equivalent mass m^* are defined as

$$\beta = \frac{\ln e}{\sqrt{(\ln e)^2 + \pi^2}} \tag{6}$$

$$S_n = 2E^*\sqrt{R^*\delta_n} \tag{7}$$

$$\frac{1}{m^*} = \frac{1}{m_i} + \frac{1}{m_j}, \tag{8}$$

where e is the coefficient of restitution (CoR).

The tangential force (F_t) also has two terms: a spring force $F_t^s$and a damping force F_t^d:

$$F_t = F_t^s - F_t^d\,. \tag{9}$$

The spring force is defined as a function of the tangential overlap distance of two particles, δ_t

$$F_t^s = -S_t\delta_t, \text{ and } \left|F_t^s\right| \le \mu\left|F_n^s\right| \tag{10}$$

where μ is the friction coefficient and the tangential stiffness S_t is calculated by using

$$S_t = 8G^*\sqrt{R^*\delta_n}, \tag{11}$$

with the equivalent shear modulus G^* is defined as

$$\frac{1}{G^*} = \frac{2(2-\nu_i)(1+\nu_i)}{E_i} + \frac{2(2-\nu_j)(1+\nu_j)}{E_j}. \tag{12}$$

In addition, the damping force F_t^d is given by

$$F_t^d = -2\sqrt{\frac{5}{6}}\beta\sqrt{S_t m^*}\upsilon_t, \tag{13}$$

where v_t is the tangential component of the relative velocity between two particles.

The geometry of the chamber and the processing parameters are listed in Table 1. The numerical values of these parameters are chosen using references [40–46]. The materials of the shot, sonotrode, chamber and target are AISI 304, Ti6Al4V, hardened steel and AISI 316 stainless steel, respectively. As listed in Table 2, the material parameters are determined by using relevant literature and material related databases [47–50].

In the real treatment, the initial positions of the shot particles are unknown. In our DEM model, the shot particles are initially inserted on the surface of the sonotrode, completely randomly without overlap, which can be done by executing the self-contained command in the LIGGGHTS code. The initial velocities of all shot particles are set to zero.

2.2. Modelling rough sonotrode surface

As shown in Fig. 2(a), which comes from the laboratory at UTT, the observed sonotrode surface is not completely smooth after extensive use (also observed in [51]), which can be implemented in the DEM model by replacing a smooth wall (a particle with infinite radius) with a rough wall (particles with finite radii). Two different methods can be employed to create a rough wall: (1) constructing a lattice of particles; (2) creating one layer of spheres by reading the data file containing position information of particles. For the sake of simplicity while being capable of controlling different types of rough surface, the second method is selected here. The adopted method introduces several parameters, such as lattice arrangement, sphere diameter and the spacing between two closest spheres. In this work, a hexagonal arrangement pattern is employed because it creates the closest packing of equal spheres, as illustrated in Fig. 2(b).

To make sure there is no gap among spheres assembling the sonotrode surface, a condition for the maximum distance between two closest spheres is imposed as $d_{max} = \sqrt{3}r$, where r is the radius of sonotrode spheres. The surface of the rough sonotrode is defined as the plane consisting of intersection points. The distance D between the top target and the sonotrode is illustrated in Fig. 2(d). Then, the root mean square (rms) roughness of the sonotrode S_q, can be calculated using the

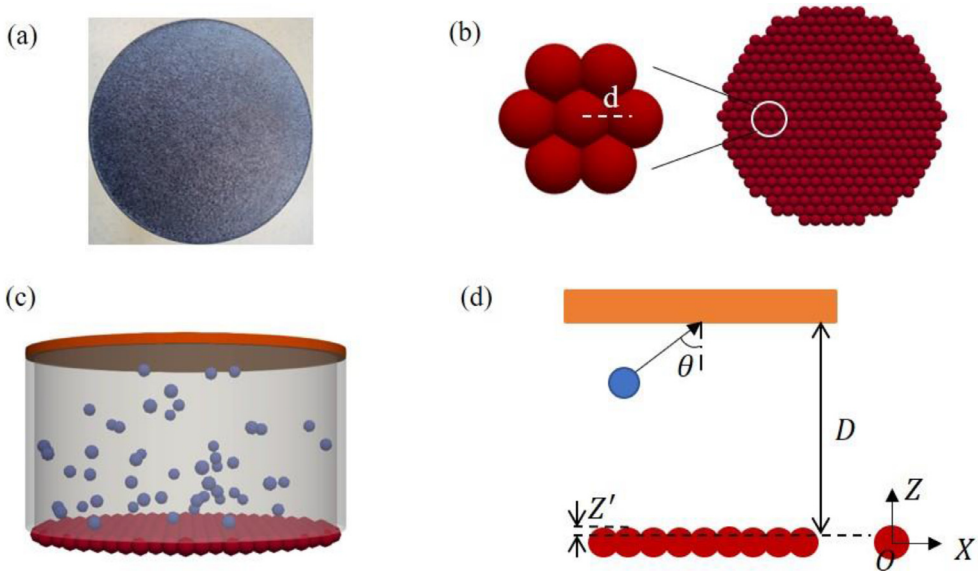

Fig. 2. (a) Sonotrode surface after extensive use; (b) The hexagonal arrangement of spheres over the whole sonotrode surface; (c) A snapshot of the simulation; (d) 2D schematic of the SMAT process.

Table 3
Simulation cases and their parameters for roughness study.

Case name	r (mm)	d (mm)	Roughness – RMS (mm)	Treatment duration (s)
r05d187	0.5	1.87	0.15	150
r10d173	1	1.73	0.30	150
r15d260	1.5	2.60	0.45	150
r20d346	2	3.46	0.60	150
r20d200	2	2	0.15	150
r20d100	2	1	0.04	75
r25d346	2.5	3.46	0.40	60
r30d346	3	3.46	0.31	60
r35d346	3.5	3.46	0.26	60
r02d026	0.15	0.26	0.05	30

following formula:

$$S_q = \sqrt{\frac{1}{A}\iint_A z'^2 dx dy}, \tag{14}$$

where z' is the peak value of the sonotrode surface.

$$z' = z - \sqrt{r^2 - \left(\frac{d}{2}\right)^2}. \tag{15}$$

The visual animations of the motion of shot inside the chamber can be achieved with the post-processing software ParaView by outputting the information of the shot, spheres and walls. The collision pairs always involve one shot with another shot, static and moving walls. In our model, only collisions between walls (chamber, sonotrode and target) and shot particles are recorded to reduce the size of output files. To ensure that no contact information is missed, the instant contact coordinates of each shot-target contact and the shot velocity at the contact point are recorded at each time step. This raw data can afterwards be delivered to Mathematica scripts to extract the detailed information of spatial and statistical impact distributions.

2.3. Simulation cases

The model considers a cylinder chamber, made of hardened steel, in which 50 AISI 304 spheres are randomly placed on the top of the rough sonotrode. The parameters that have been kept constant in this model are listed in Tables 1 and 2.

Surface topography is usually defined by the three characteristics of lay, waviness and roughness. For these typical roughness indices, flat surfaces with isotropic pattern (hexagonal array) are employed in this model. Though the regular hexagonal patterns are adopted for simplicity in this study, the arrangement of the patterned surfaces reflects typical rough surfaces of sonotrode, in terms of waviness and roughness. The roughness parameters of the sonotrode that affects the simulation results are the radius of the spheres, r, and the distance between two closest spheres, d. Table 3 gives the values attributed to these parameters, the resulting roughness parameter and the duration of the treatment for each simulation case performed in this study.

To optimize SMAT, it is important to study the effects of the processing parameters such as the vibration amplitude A and frequency f of the sonotrode, the radius r_0 of shot, the number N of shot and the distance D between the sonotrode and the target. The ranges of values for each of these parameters have been chosen to reproduce industrial application values. These ranges were obtained based on the information given by Badreddine et al. [41]. Table 4 presents the values of these parameters. For this parametric study, the parameters describing the roughness of the sonotrode are those of case r20d346.

3. Simulation conditions

3.1. Coefficient of restitution (CoR)

During SMAT, the contact area of the target is impacted repeatedly by shot. Plastic deformation and the resulting compressive residual stress produced by impacts will increase the hardness of the target through strain hardening after each impact. The CoR, which can be defined as the velocity ratio before and after impact [52], is an important indicator of the energy loss and the effect of strain hardening due to the plastic deformation of the target during the shot-target collisions. CoR

Table 4
Processing parameters values used in the parametric study (Case r20d346).

Sonotrode		Shot		Chamber
Vibration amplitude A (μm)	Vibration frequency f (kHz)	Radius r_0 (mm)	Number N	Distance D (mm)
10	20	1.5	50	38
25	20	1.5	50	38
50	20	1.5	50	38
25	10	1.5	50	38
25	20	2	50	38
25	20	3	50	38
25	20	1.5	100	38
25	20	1.5	150	38
25	20	1.5	50	20
25	20	1.5	50	60

is a function of shot velocity (i.e., CoR decreases with increasing impact velocity), shot material, angle of impacts, target material hardness etc. Here, we only adopted the basic rate-independent Tsuji model, which has been implemented in various DEM methods. The indent size after shot-target impact is also an essential parameter for the calculation of the coverage rate. However, the DEM method cannot account for the deformation process caused by the impact on the sonotrode surface. To overcome this problem, a FEM model is used for analyzing the deformation of the target due to shot impacts and the results of the simulations will be used in the DEM simulations.

A three-dimensional FEM of multiple impacts is built to calculate the indent size and rebound velocities of shot after impact. The indent size is defined as the horizontal distance measured from the highest peak to the lowest valley after the shot impact. The elastic modulus, Poisson's ratio and density of the shot and target materials are kept consistent with the values used in the DEM model, shown in Table 2. In the FEM simulation, the target is modeled as an elastic-plastic material by using a Johnson-Cook (J-C) material hardening behavior described by the following constitutive equation:

$$\sigma_{eq} = (A + B\varepsilon^n)\left[1 + C\ln\left(\frac{\dot{\varepsilon}}{\dot{\varepsilon}_0}\right)\right]\left[1 - \left(\frac{T - T_0}{T_m - T_0}\right)^m\right] \tag{16}$$

where ε is the plastic strain, $\dot{\varepsilon}$ the strain rate, $\dot{\varepsilon}_0$ the reference plastic strain rate, T the temperature of the target, T_m the melting temperature of the target, T_0 the room temperature, A the yield strength, B the hardening modulus, C the strain rate sensitivity coefficient, n the hardening coefficient and m the thermal softening coefficient. Table 5 presents the values for these parameters used in our simulations. These values were obtained from the literature [47].

Table 5
Material constants for the J-C constitutive model.

$\dot{\varepsilon}_0$ (/s)	T_m(°C)	T_0(°C)	A (MPa)	B (MPa)	C	n	m
200	1399	20	280	1750	0.1	0.8	0.85

Repeated impacts with identical initial velocities at the identical location are performed. The FEM model is presented in Fig. 3(a), with a shot radius of 1.5 mm. To have a realistic idea of how many impacts should be simulated, we use the values from the DEM simulation case r20d346. For that particular simulation, the treatment duration is 150 s, during which 220,502 impacts occur on the target. Taking the indent radius as 0.275 mm, each point on the target surface is likely to be hit 13 to 14 times in average. Seifried et al. [52] investigated the dependency of the CoR on the number of impacts and indicated that the CoR reaches a stable value after several impacts. Here we use an exponential function to fit the simulation result for the CoR and obtain the stable value of 0.69, as presented in Fig. 3(b). The CoRs of shot-shot, shot-chamber, shot-sonotrode are assumed to be 0.8.

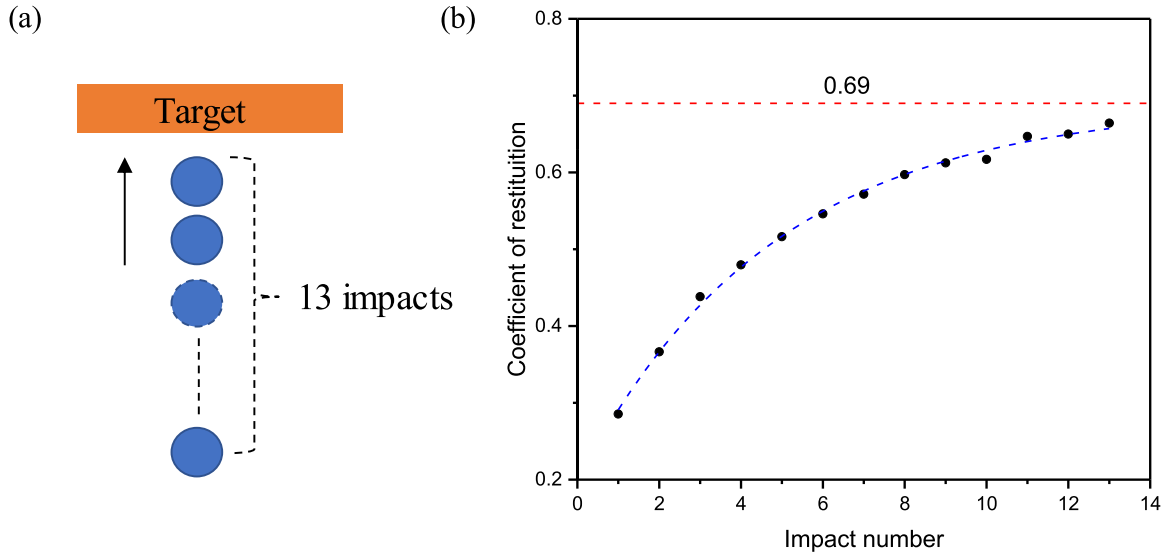

Fig. 3. (a) FEM simulation results using 13 impacts at the same position on the target surface. (b) CoR evolution with the impact number. The CoR varies due to the strain-hardening effect of the target material. The stable CoR value is found to be 0.69 after fitting the data with an exponential law (shown as the blue dashed trend line).

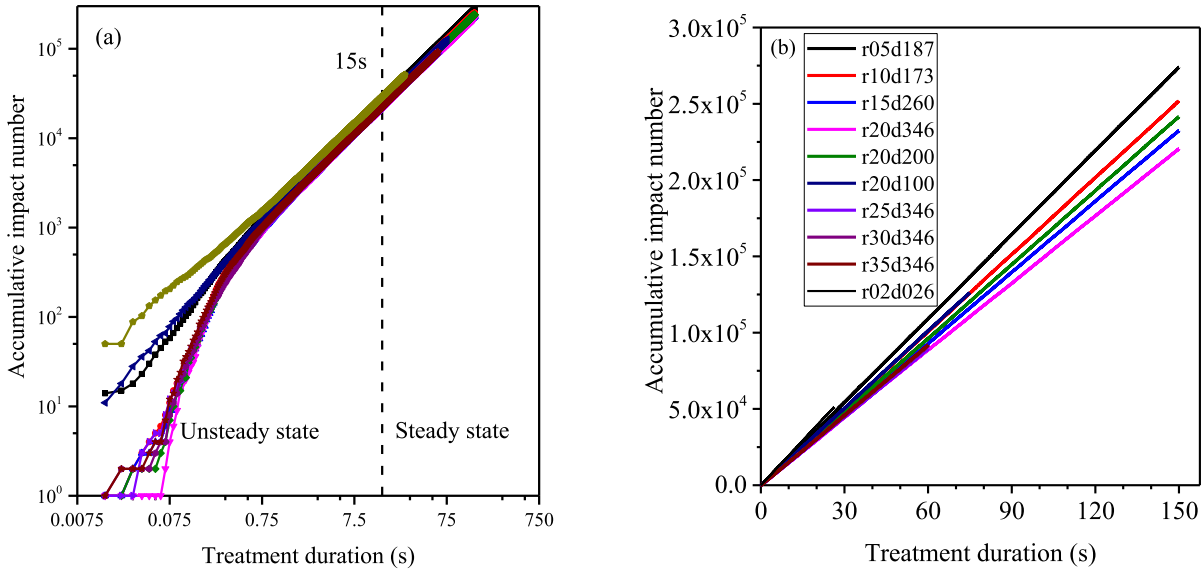

Fig. 4. Accumulative impact number on the target: (a) in a log-log scale, (b) a linear scale.

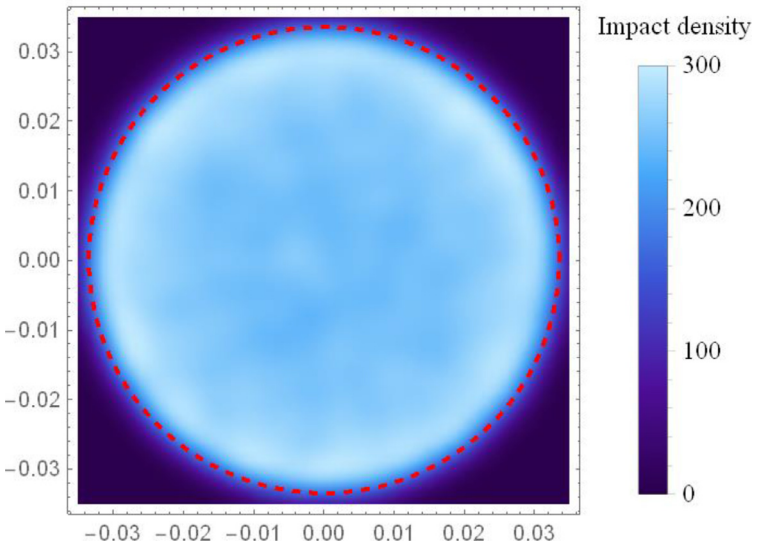

Fig. 5. Spatial impact density on the target for case r20d346. The red dashed circle represents the limit of shot interaction with the target, referred as the indentation boundary.

3.2. Steady state

At the beginning of the DEM simulations, all the shot particles are immobile on the sonotrode surface. When the sonotrode starts vibrating, there is a small space between the shot and the sonotrode. Once the shot obtained an initial velocity owing to gravity, the motion of the shot starts. After several shot-sonotrode collisions, the shot gains enough energy to impact the target. The process of energy accumulation is regarded as unsteady and this phenomenon can also be observed during SMAT experiments [53]. For all the considered cases described in the Table 5, the influence of the roughness parameters on the onset of steady state is investigated. As illustrated in Fig. 4(b), the accumulated impact number can be considered to vary linearly with the of treatment duration. The curves on a log-log scale in Fig. 4(a) highlight the onset of steady state varying with impact number per second. Cases r05d187 and r20d026 achieve their steady state within the shortest time, due to the shot in these two cases having a greater impact number per second than for the other cases.

The unsteady state shows the qualitative description of the shot dynamics within the first several seconds of treatment duration. At the beginning of the treatment, the velocity of the shot is zero. After several collisions with the vibrating sonotrode, the shot particle obtains enough kinetic energy to impact the target. The transition from unsteady state to steady state depends on the impact rate, which is determined by the roughness parameters. Therefore, it is of great significance to evaluate this transition time to guarantee a reliable analysis on the effect of the roughness parameters. It has been observed throughout all the cases that the steady state is always reached after an initial treatment duration of 15 s. Therefore, the results presented and discussed below are of the data obtained once steady state has been reached.

4. Results and discussion

The results presented in the following sections focus on the statistical and spatial distributions of the impact velocity, both in terms of magnitude at impact and trajectory direction, as the velocity directly affects the resulting surface topography, residual stresses and microstructure of the treated targets.

4.1. Spatial impact distribution and coverage evolution

The DEM model gives access to the coordinates of each impact position, making it possible to extract a spatial impact distribution. The spatial impact density for case r20d346 is presented in Fig. 5. From that

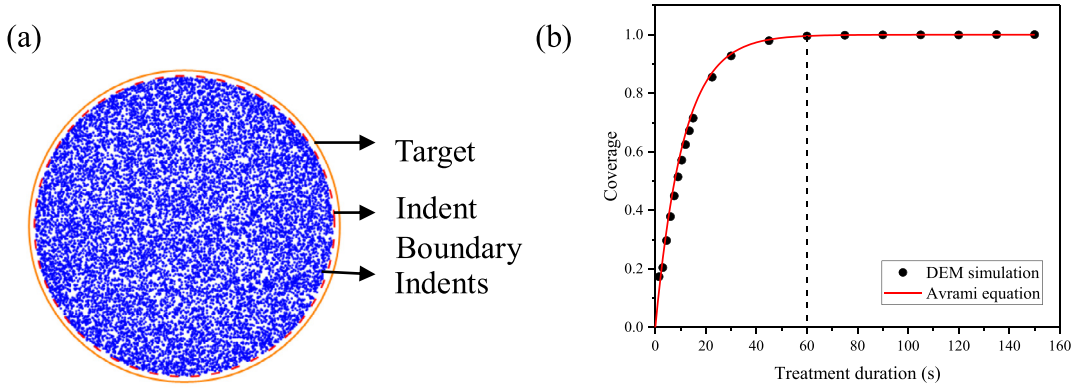

Fig. 6. (a) Simulated coverage area for case r20d346 that has 14,752 impacts. Each blue dot represents an indent location. The dashed circle represents the indent boundary. The solid line represents the inner diameter of the chamber. (b) Coverage vs. treatment duration. The dashed line represents the time for reaching full coverage.

image, one can clearly see that there is an almost uniform distribution of the impacts in the center and at the edge of the target. However, there is a ring close to the edge of the target where the impact intensity is lower than on the rest of the target surface. Due to the size of the shot, there is a gap between the impacted area and the target size (defined as the inner chamber circle) that can clearly been see on Fig. 6(a).

Coverage is an important indicator for treatment quality and performance. Insufficient coverage may cause component failure by creating regions with low strength while excessive coverage may lead to surface damage [54]. The indentation size is essential to evaluate the coverage evolution. In practice, the indentation size varies with the shot velocity, impact angle and material properties of the target and the shot. In this study, the indent size is only used to describe the time evolution of the coverage area. Cao et al. [55] verified that though the vertical impact velocity determines the indent size, the coverage rate is directly related to average indent size. To simplify the calculations, the current model only considers the average shot velocity in the vertical impact direction and assumes that all the indents have the same diameter. In this model, the indentation radius is 0.275 mm, value obtained from FEM simulations for a single impact with a shot diameter of 1.5 mm. Using Mathematica and the data obtained from the DEM simulations, the coverage for each simulation is calculated assuming a 0.275 mm radius circular indent centered around the coordinates of every single impact position, as depicted in Fig. 6(a). The relationship between coverage and the accumulative impact number is supposed to follow an Avrami law [56]. At first, the indents are likely to appear scattered without much overlap and then the coverage rate increases almost linearly with treatment duration. As the surface coverage increases, the rate of coverage decreases since the probability of overlap increases. According to Hassani-Gangaraj et al. [57–59], the coverage can be expressed as function of the ratio of indented area to total area, A_r,

$$C = 1 - e^{-A_r} \tag{17}$$

$$with\ A_r = \frac{N\pi r_d^2}{\pi R_t^2} = \frac{r_d^2}{R_t^2} nt \tag{18}$$

where, N is the accumulative impact number, r_d the radius of a single indent, R_t the radius of the target, n the impact rate, and t the treatment duration.

The impact rate, here, is defined as the average impact number per second. The impact rates for all the simulated cases are listed in Table 6. The Avrami equation, Eq. (17), is plotted against treatment duration using the impact rate of case r20d346 in Fig. 6(b) as a solid red line. In this figure, the coverage in evolution obtained via the DEM model is compared with the empirical equation. As this figure clearly shows, the simulated coverage represented by the black solid dots is in agreement with the Avrami equation.

Table 6
Impact rates for all simulation conditions.

Case Name	Impact rate (s^{-1})
r05d187	1824.7
r10d173	1683.1
r15d260	1558.9
r20d346	1475.2
r20d200	1610.2
r20d100	1683.8
r25d346	1496.8
r30d346	1522.9
r35d346	1541.5
r02d026	1951.2

4.2. Impact angle distribution

The DEM model provides information on the direction of impact of the shot which can be described through the value of an impact angle. In the model, an impact angle θ equals to 0° means a vertical impact, while a value of 90° represents a horizontal impact, as shown in Fig. 8(c). The distribution of the impact angles can be statistically described using density distribution function, or probability distribution function (PDF).

Although the impact density close to the chamber wall is lower compared to anywhere else on the target based on the results showed in Fig. 5, the spatial distribution of impact angle is homogeneous over the entire surface of the target and the impact angle values range from 0.53° to 89.26°. Such a uniform distribution across the target surface should produce a homogeneous surface roughness for the treated target samples.

Fig. 7 presents the statistical distributions of the impact angles for all the simulated cases. The roughness of the sonotrode strongly affects that statistical distribution. With the same sphere radius used to create the sonotrode surface (cases r20d346, r20d200, and r20d100), the average impact angle increases with increasing sphere spacing. Using the same sphere spacing (cases r20d346, r25d346, r30d346, and r35d346), the average impact angle decreases with increasing sphere radius. This means that the average impact angle is positively correlated to sphere spacing (surface wavelength), but negatively correlated to sphere radius (roughness slope). However, there is no clear correlation between the average impact angles and the surface roughness of the sonotrode.

The primary parameters that determine the surface roughness of the sonotrode are (i) sphere radius and (ii) sphere spacing. As Fig. 8(c) shows that, assuming no obstacles prevent the trajectory of the shot

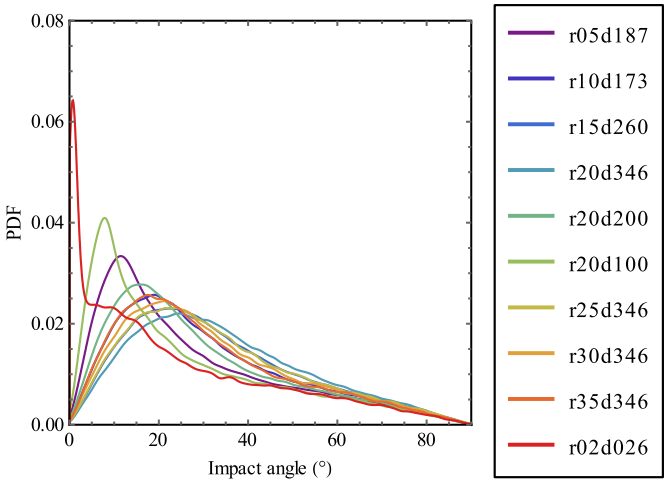

Fig. 7. Statistical distributions of the impact angles for all the simulates cases.

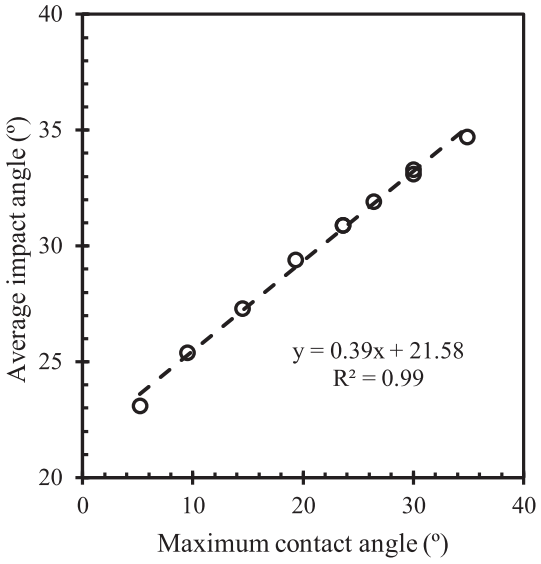

Fig. 9. Average impact angles vs. maximum contact angles between shot and spheres.

towards the target (chamber wall or other shot) and no tangential component of relative velocity between shot and sphere, and ignoring the trajectory deviation caused by the decreasing vertical velocity due to gravity (Δv around −0.06 m/s), the impact angle of the shot is identical to the incident angle of the shot which is determined by the contact angle between shot and spheres representing the surface of the sonotrode.

As shown in Fig. 8(a), the maximum contact angle between shot and spheres, obtained for a given simulation, is achieved when the shot is located at the center point between three touching spheres. As we can see from Fig. 8(b), the maximum contact angle between shot and sphere, θ_m, can be calculated by using the following formula:

$$\theta_m = \arcsin\frac{d}{\sqrt{3}(r+r_0)} \tag{19}$$

where r_0 is the radius of the shot.

The relation between the maximum contact angles between shot and spheres and the shot impact angles with the target, for all the simulations, is plotted in Fig. 9. That plot shows the strong linear correlation that exists between these two angles. Such correlation connects the surface topological features to the resulting impact angle distribution. Because of the tangential component of the relative velocity before shot-sphere collisions, the bouncing angle of shot is larger than the contact angle, shot which explains why the value of the average impact angle is larger than the maximum contact angle between shot and spheres.

4.3. Impact velocity distribution

Impact velocity is a key factor in these simulations as it can be used as input data for subsequent detailed FEM simulations to predict the residual stresses and surface roughness of the target. The DEM simulations provide three velocity components in the *x*, *y*, and *z* directions just before the shot-target collision. The total velocity can be obtained using these three velocity components. As residual stresses are strongly correlated to velocity component in the z-direction, or vertical velocity [41], our following discussion will focus on the vertical velocity distribution.

The spatial distribution of vertical impact velocity is uniform over the entire target surface and the values range wide from 0.02 to 10.33 m/s. For all cases, the vertical impact velocity with nearly uniform and high probability ranges from 2 to 7 m/s. Such a uniform distribution across the target should produce a homogeneous compressive residual stress field distribution within the target sample after the SMAT treatment.

The statistical distributions of the vertical impact velocity of all the simulated cases are plotted in Fig. 10. These distributions are seriously influenced by the roughness parameters of the sonotrode surface. The average vertical velocities decrease with increasing sphere spacing for the same sphere radius (i.e., cases r20d346, r20d200, and r20d100 have the same sphere radius), however, the average vertical velocity increases with increasing sphere radius for the same sphere spacing (cases r20d346, r25d346, r30d346, and r35d346). That means that the average vertical impact velocity is negatively correlated to the sphere spacing, but positively correlated to sphere radius. Here again, there is no direct correlation between average vertical velocity and surface roughness. Due to the scattered maximum vertical velocities for different treatment durations, here we just discuss the average values of the vertical velocity.

In the Hertzian contact model, the force between shot and sonotrode spheres has a spring component and a damping component on both

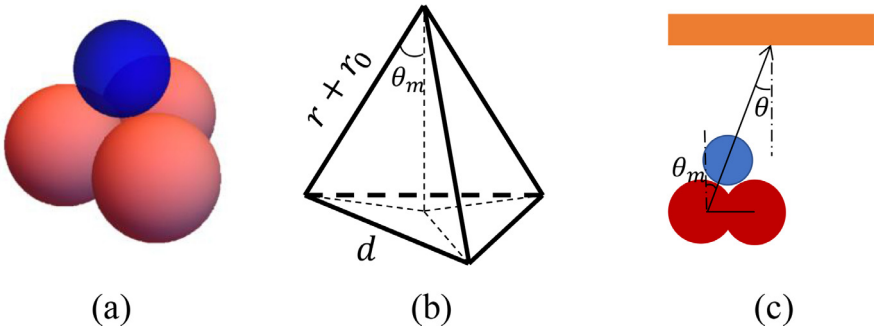

Fig. 8. (a) Schematic diagram of shot-sphere position. (b) Sketch describing the maximum contact angle as a function of parameters describing the roughness of the sonotrode and the shot. (c) Schematic diagram showing the relationship between the maximum contact angle between shot and spheres and the shot impact angle with the target.

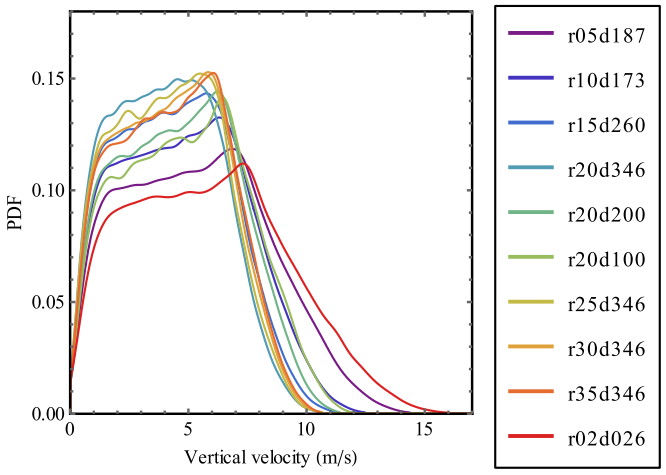

Fig. 10. The statistical distributions of the vertical impact velocity of all the studied cases.

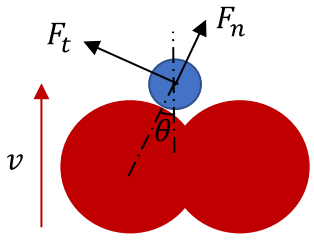

Fig. 11. Diagram of shot-sonotrode collision.

normal and tangential directions. The amplitudes and frequencies of the sonotrode vibrations are the same in all our roughness effect study, which means the total energy that the system can obtain is the same for all these cases. Therefore, the difference in the average impact velocity between all the simulations is caused by the damping components.

As shown in Fig. 11, when the shot gets into contact with the sonotrode spheres at an angle θ, the damping component of the contact force in the vertical direction is expressed as:

$$F^d = F_n^d \cos\theta + F_t^d \sin\theta \ . \tag{20}$$

Combining Eqs. (5) and (13), we can get

$$F^d = 2\sqrt{\frac{5}{6}}\beta\sqrt{S_n m^*}\, v_n \cos\theta + 2\sqrt{\frac{5}{6}}\beta\sqrt{S_t m^*}\, v_t \sin\theta \ . \tag{21}$$

Assuming the initial velocity of the shot is zero, then the normal component of the relative velocity between shot and sonotrode v_n and the tangential component of the relative velocity between shot and sonotrode v_t can be given by:

$$v_n = v\cos\theta \tag{22}$$

$$v_t = v\sin\theta \ . \tag{23}$$

Substituting Eqs. (7), (11), (22) and (23) into Eq. (20), and simplifying the expression of F^d:

$$F^d = 2\sqrt{\frac{5}{3}}\beta\left[(m^*)^{\frac{1}{2}}(R^*)^{\frac{1}{4}}\left(\sqrt{E^*}\cos^2\theta + 2\sqrt{G^*}\sin^2\theta\right)\right] v\,(\delta_n)^{\frac{1}{4}} \ . \tag{24}$$

We know from the impact angle section that the contact angle is correlated to the maximum contact angle between shot and spheres. In our model, we give the contact angle θ the value of the maximum contact angle θ_m. Here, we name the damping factor in the vertical direction c and exclude the constant $2\sqrt{\frac{5}{3}}\,\beta$, then the analytical expression of c is simplified as:

$$c = (m^*)^{\frac{1}{2}}(R^*)^{\frac{1}{4}}\left(\sqrt{E^*}\cos^2\theta_m + 2\sqrt{G^*}\sin^2\theta_m\right) \ . \tag{25}$$

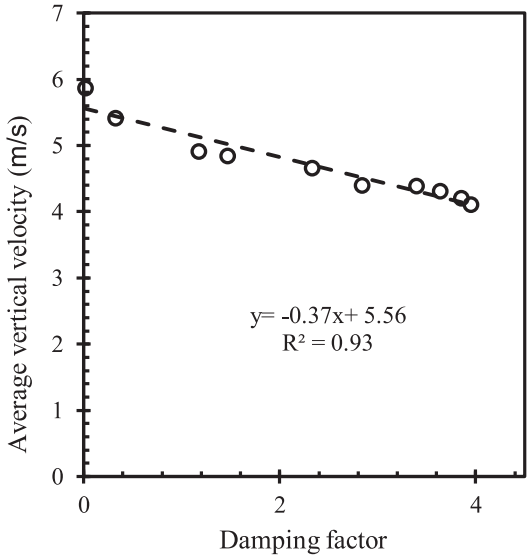

Fig. 12. Average vertical velocity vs. defined damping factor (c).

This parameter c can be calculated by using the material parameters (shown in Table 2) and the sonotrode geometry parameters (shown in Table. 3). Fig. 12 shows the relationship between the damping factor c and the average vertical velocity.

Finally, in Fig. 13(a), the joint density distribution of impact angles and vertical velocities is presented. The higher vertical velocity is related to smaller impact angle, which corresponds to shot particles with almost direct trajectories between the sonotrode and the target, without colliding with chamber walls, and therefore, less kinetic energy is lost. However, when the collision number increases, the shot is more likely to change its trajectory, resulting an increasing impact angle. Fig. 13(b) shows the relationship between average vertical velocity and impact rate. With the different sonotrode roughness but same processing parameters, the impact rate linearly increases with the average vertical velocity.

4.4. Sonotrode amplitude and frequency

The effect of the amplitude and frequency of the sonotrode were also investigated. Specifically, three different amplitude A =10, 25, 50 μm, and two different frequency f =10 and 20 kHz were studied. Fig. 14(a) shows the distribution of the impact angle for different amplitudes A and frequencies f. The effect of the amplitude A and frequency f on the distribution of the impact angle was found to be negligible. The inset of Fig. 14(b) shows the distribution of the vertical velocity for different amplitudes A and frequencies f. As shown in Chan et al. [27], a linear relationship exists between the sonotrode amplitude and the maximum velocity the shot can achieve. The maximum vertical velocity increases with the amplitude A and frequency f; these two parameters define the input energy of the SMAT process. The motion equation of the sonotrode is expressed as $y = A\sin(2\pi ft)$, and thus the vibration velocity of the sonotrode is $v = 2\pi fA\cos(2\pi ft)$. The normalized vertical velocity of the shot is obtained by dividing the vertical velocity of the shot by the coefficient fA, which gives an information on the maximum vibration velocity of the sonotrode. Fig. 14(b) shows the distribution of the normalized vertical velocities for different amplitudes A and frequencies f. It shows that the amplitude A and frequency f of the sonotrode have little effect on the distribution of normalized vertical velocities assuming that the same amount of energy is given to the system.

4.5. Shot diameter and number

The effects of the shot diameter (d) and the number of shot (n) were investigated. The shot diameter was given the value 3, 4 or 5 mm and

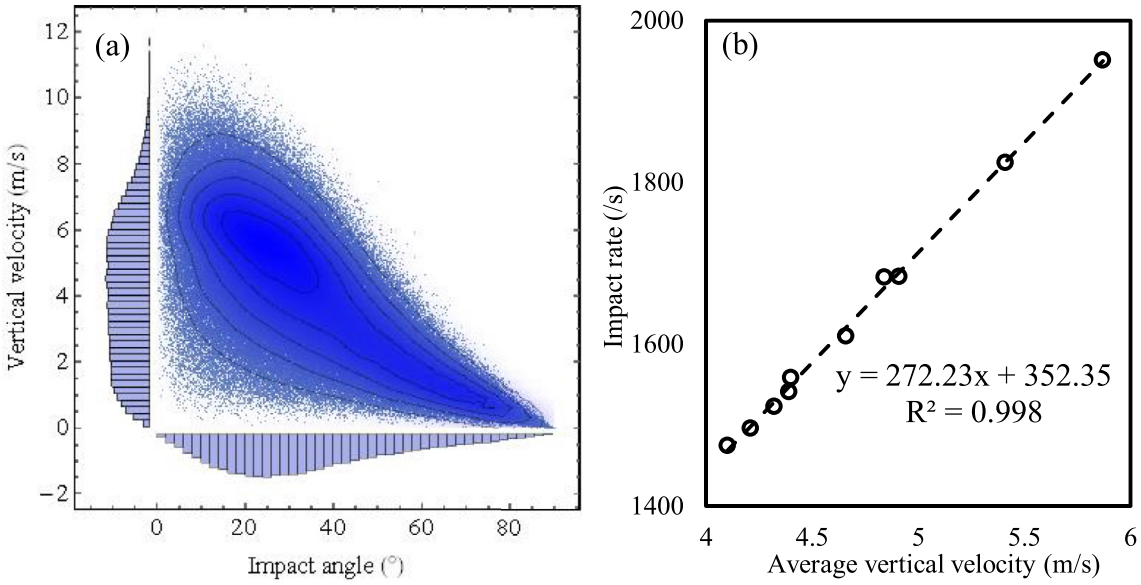

Fig. 13. (a) The joint distribution of impact angles and vertical velocities for case r20d346 and (b) average vertical velocity vs. impact rate.

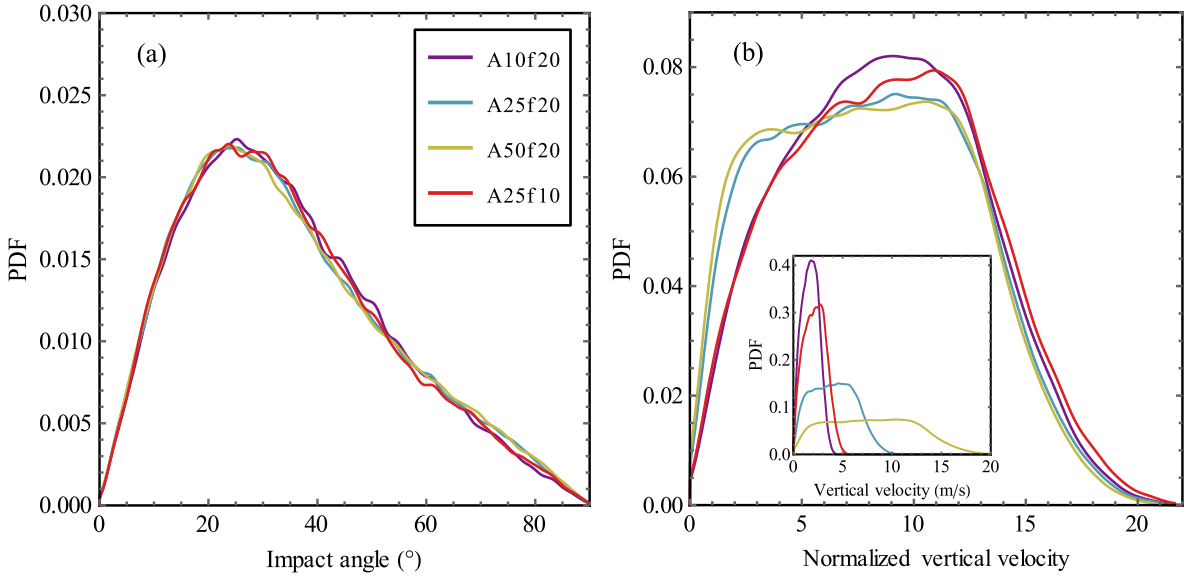

Fig. 14. Statistical distribution of (a) the impact angle, (b) the normalized vertical velocity and the vertical velocity (the inset figure) for different amplitudes *A* and frequencies *f*.

while the total number of shot was given the value 50, 100 or 150, respectively. Fig. 15(a) shows the distribution of the impact angles for different shot diameter *d* and number of shot *n*. These two parameters did not influence much the distribution of the impact angles. Fig. 15(b) shows the distribution of the vertical velocities for different shot diameter *d* and number of shot *n*. We can see that the average vertical velocity decreases with increasing shot diameter *d* and number of shot *n*. The probability of collisions within the chamber is dependent on the total surface area of the shot, which is equal to $S = n\pi d^2$. Fig. 16 shows the average vertical velocity decreases when the total surface area of the shot increases within the range of the simulated cases.

4.6. Chamber height and treatment duration

The effects of the chamber height and treatment duration were investigated using the following parameters: the chamber height *H* was given the following values: 20, 30, 34, 38 and 60 mm, and the treatment duration *t* was given the following values 25, 50, 75 and 150 s. Fig. 17 shows the distributions of impact angles and vertical velocities for different chamber height *H* and treatment duration *t*. The chamber height *H* and treatment duration *t* have no notable influence on the distribution of the impact angles and vertical velocities. However, the impact rate increases with decreasing chamber height H, due to the fact the total travel distance decreases for lower chamber height. The linear relationship between impact rate and reciprocal chamber height H is shown in Fig. 17(e).

The impact details between shot and target are essential to accurately predict the deformation of target. However, due to the high-speed shot dynamics, it is hard to directly observe the detailed and accurate trajectory of shot by experiments. In the previous studies, without the full understanding of impact information, such as impact locations, impact angles and impact velocity, researchers tend to assume the impact events

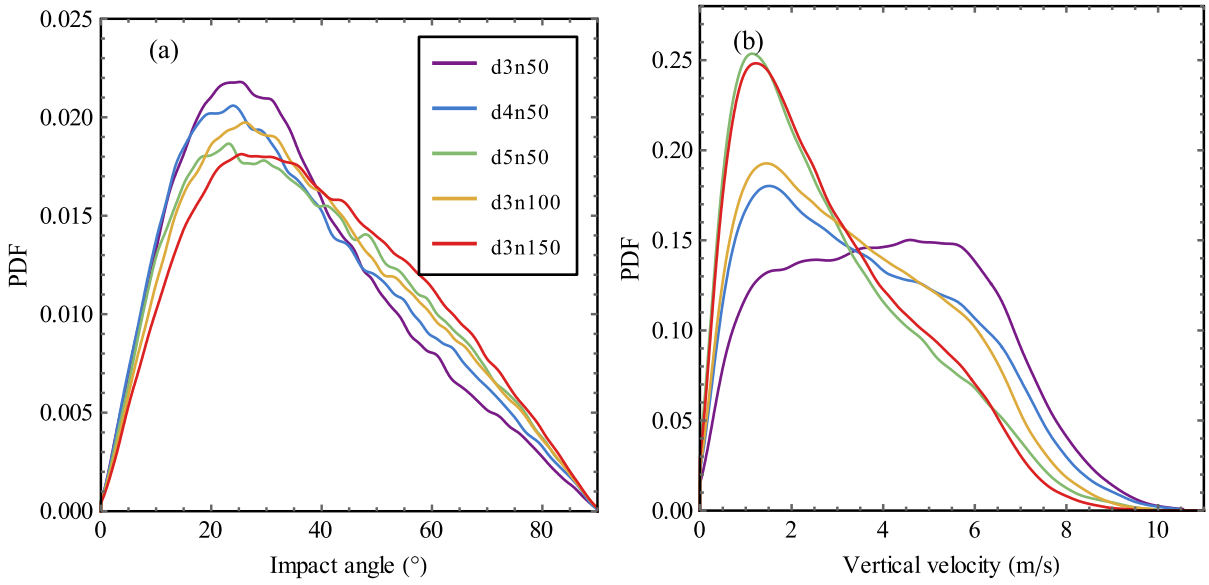

Fig. 15. Probability distribution functions (PDFs) of (a) impact angle and (b) vertical velocity for different shot diameter *d* and number of shot *n*.

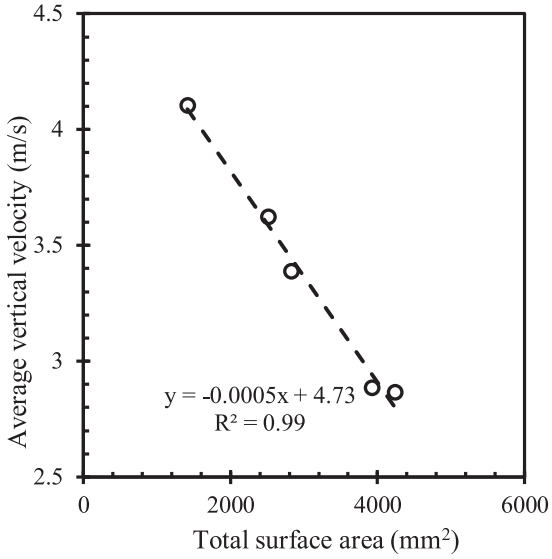

Fig. 16. Average vertical velocity vs. total surface area of the shot. The total area is a function of the shot diameter *d* and the number of shot *n*.

are uniformly distributed on the target [55] or use specific values [38], which reduces the reliability of the computation and limited the promotion and development of SMAT. Although Badreddine et al. [41] simulated the shot dynamics with smooth sonotrode by imposing random initial impact angle to the shot, the impact directions were closed to normal after a period of treatment time, which goes against with multi-directional and random characteristics of SMAT processes. To achieve high fidelity of predicting these substantive characteristics, the current numerical model presented here adopted the rough-sonotrode, with controllable surface features. The effect of rough-sonotrode as well as processing parameters on the SMAT result have been investigated, and the factors that affect the impact angle, vertical velocity and impact rate have been identified. Our analytical method provided the foundation to understand the procedure of SMAT. In principal, the developed numerical framework can also be generalized on other metallic materials by applying the corresponding material properties.

5. Conclusions

This paper presents a numerical framework combining discrete and finite element methods for modelling ultrasonically assisted SMAT processes, highlighting the effects of sonotrode surface topology. The proposed method allows simulations of the shot dynamics, and especially provides detailed impact information on the treated target, for various cases with different sonotrode surface topology. Before performing the DEM simulations, FEM simulations of multiple impacts at the same location have been carried out to obtain the coefficient of restitution (CoR). To ensure the reliability of the DEM analysis of SMAT processes, the data are all extracted from the steady state regime.

Through the systematically analysis, different impact statistics have been found to be connected to the surface characteristics of the sonotrode, as well as other key processing parameters during the SMAT treatments. Mechanistic models for predicting shot coverage, impact angle and velocity distributions have been proposed, including the geometrical and material features of shot particles, sonotrode, and processing conditions. The most important results can be drawn as follows:

(1) Sonotrode roughness affects the statistical distribution of impact angle and impact velocity. For the same roughness, the average impact angle increases with increasing waviness. For the same waviness, the average impact angle increases with decreasing roughness. The average vertical velocity decreases with increasing damping factor c, which is caused by increasing waviness and decreasing roughness, as proposed in Eq. (25).
(2) Regarding the chamber geometry, the impact rate decreases when the chamber height increases. The chamber height has no effect on the distribution of impact angle and impact velocity. With increasing shot number and shot size, the resulting average vertical velocity decreases.
(3) For processing conditions, including the amplitude and frequency of sonotrode, and the treatment duration, a linear relationship exists between the maximum vibration velocity of the sonotrode and the maximum impact velocity of the shot. For treatment duration, after reaching the steady state, the spatial impact distribution is uniform, and the simulated coverage evolution follows Avrami's equation.

These proposed predictive models, establishing the linkage between impact statistics and sonotrode surface features, could be used to guide the tailored design of SMAT in the future.

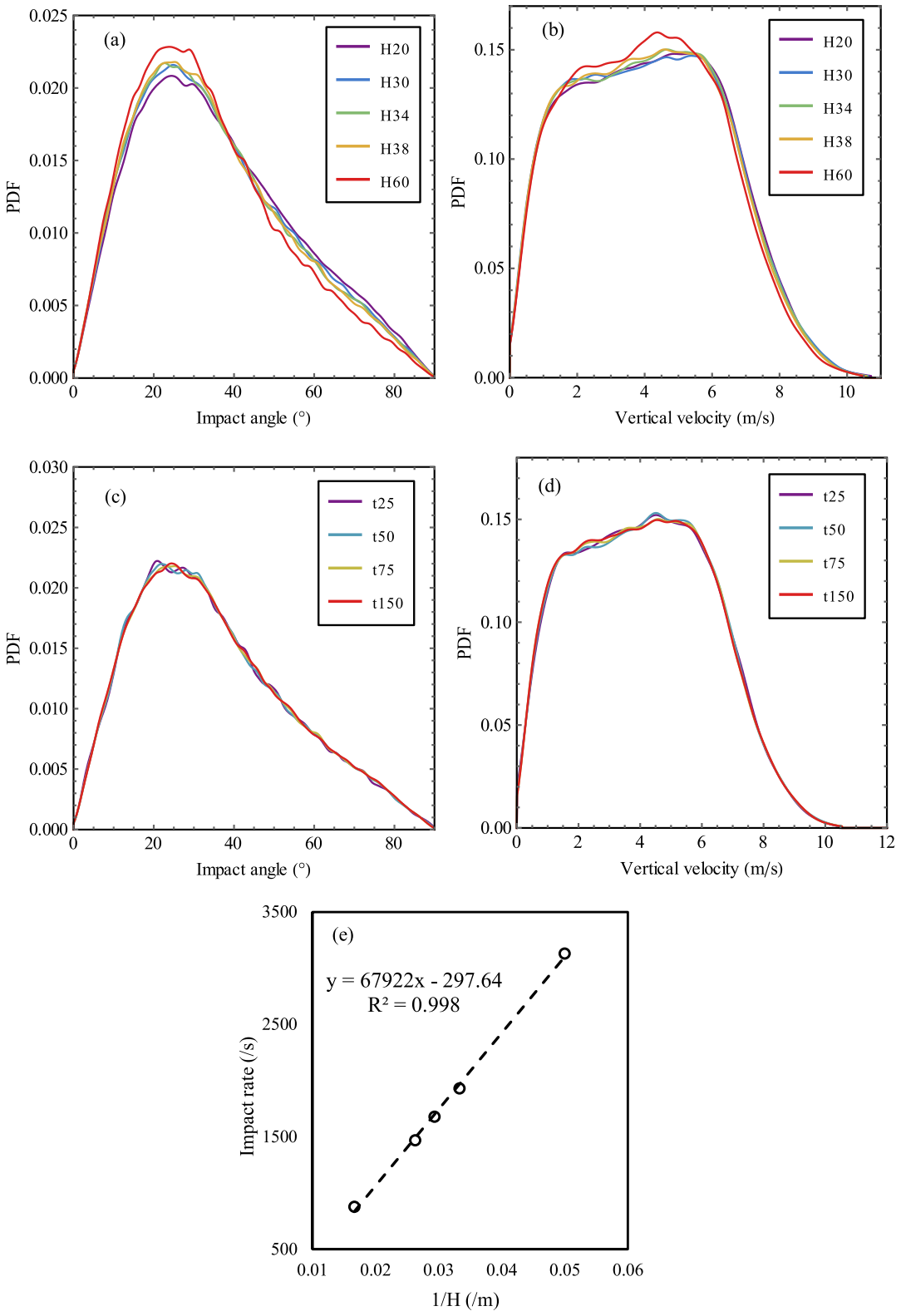

Fig. 17. Statistical distributions of (a) impact angles for different chamber height *H*, (b) vertical velocities for different chamber height *H*, (c) impact angles for different treatment duration *t*, (d) vertical velocities for different treatment duration *t* and (e) impact rate vs. the reciprocal of chamber height.

Acknowledgement

This work was financially supported by The University of Sydney SOAR Fellowship. The authors acknowledge the support from USYD-SJTU Partnership Collaboration Awards. GP acknowledges the UTT for providing financial support for her stay at the ICD/LASMIS. This research was undertaken with the assistance of resources and services from the HPC service at The University of Sydney.

References

[1] Balusamy T, Kumar S, Narayanan TSNS. Effect of surface nanocrystallization on the corrosion behaviour of AISI 409 stainless steel. Corros Sci 2010;52(11):3826–34. doi:10.1016/j.corsci.2010.07.004.
[2] Antunes RA, de Oliveira MC. Corrosion fatigue of biomedical metallic alloys: mechanisms and mitigation. Acta Biomater 2012;8(3):937–62. doi:10.1016/j.actbio.2011.09.012.
[3] Teoh SH. Fatigue of biomaterials: a review. Int J Fatigue 2000;22(10):825–37. doi:10.1016/S0142-1123(00)00052-9.
[4] Brent Bankston A, Faris PM, Michael Keating E, Ritter MA. Polyethylene wear in total hip arthroplasty in patient-matched groups. J Arthroplast 1993;8(3):315–22. doi:10.1016/S0883-5403(06)80095-1.
[5] Hammersley G, Hackel LA, Harris F. Surface prestressing to improve fatigue strength of components by laser shot peening. Opt Lasers Eng 2000;34(4–6):327–37. doi:10.1016/S0143-8166(00)00083-X.
[6] Wang X, Li YS, Zhang Q, Zhao YH, Zhu YT. Gradient structured copper by rotationally accelerated shot peening. J Mater Sci Technol 2017;33(7):758–61. doi:10.1016/j.jmst.2016.11.006.
[7] J L, Ke L. Surface nanocrystallization (SNC) of metallic materials-presentation of the concept behind a new approach. J Mater Sci Technol 1999;15:193.
[8] Mai SP, Wen CS, Lu J. Surface-modified steel sheets and corrugated panels in three-point bending. Int J Mech Sci 2018;142–143:10–20. doi:10.1016/j.ijmecsci.2018.04.024.
[9] Tao NR, Sui ML, Lu J, Lua K. Surface nanocrystallization of iron induced by ultrasonic shot peening. Nanostruct Mater 1999;11(4):433–40. doi:10.1016/S0965-9773(99)00324-4.
[10] Liu G, Lu J, Lu K. Surface nanocrystallization of 316 L stainless steel induced by ultrasonic shot peening. Mater Sci Eng A 2000;286(1):91–5. doi:10.1016/S0921-5093(00)00686-9.
[11] Tao NR, Wang ZB, Tong WP, Sui ML, Lu J, Lu K. An investigation of surface nanocrystallization mechanism in Fe induced by surface mechanical attrition treatment. Acta Mater 2002;50(18):4603–16. doi:10.1016/S1359-6454(02)00310-5.
[12] Wang C, Wang L, Wang X, Xu Y. Numerical study of grain refinement induced by severe shot peening. Int J Mech Sci 2018;146-147:280–94. doi:10.1016/j.ijmecsci.2018.08.005.
[13] Katti KS. Biomaterials in total joint replacement. Colloids Surf B Biointerfaces 2004;39(3):133–42. doi:10.1016/j.colsurfb.2003.12.002.
[14] Kohn DH. Metals in medical applications. Curr Opin Solid State Mater Sci 1998;3(3):309–16. doi:10.1016/S1359-0286(98)80107-1.
[15] Hermawan H, Ramdan D, Djuansjah JRP. Metals for biomedical applications. In: Fazel-Rezai R, editor. Biomedical engineering – From theory to applications. Rijeka: InTech; 2011. p. 40–8.
[16] Semlitsch M, Willert HG. Properties of implant alloys for artificial hip joints. Med Biol Eng Comput 1980;18(4):511–20. doi:10.1007/bf02443329.
[17] Roland T, Retraint D, Lu K, Lu J. Enhanced mechanical behavior of a nanocrystallised stainless steel and its thermal stability. Mater Sci Eng A 2007;445–446:281–8. doi:10.1016/j.msea.2006.09.041.
[18] Samih Y, Beausir B, Bolle B, Grosdidier T. In-depth quantitative analysis of the microstructures produced by surface mechanical attrition treatment (SMAT). Mater Charact 2013;83:129–38. doi:10.1016/j.matchar.2013.06.006.
[19] Proust G, Trimby P, Piazolo S, Retraint D. Characterization of ultra-fine grained and nanocrystalline materials using transmission Kikuchi diffraction. J Vis Exp 2017(122):e55506. https://doi.org/10.3791/55506.
[20] Proust G, Retraint D, Chemkhi M, Roos A, Demangel C. Electron backscatter diffraction and transmission kikuchi diffraction analysis of an austenitic stainless steel subjected to surface mechanical attrition treatment and plasma nitriding. Microsc Microanal 2015;21(4):919–26. doi:10.1017/S1431927615000793.
[21] Hu J, Shi YN, Sauvage X, Sha G, Lu K. Grain boundary stability governs hardening and softening in extremely fine nanograined metals. Science 2017;355(6331):1292–6. doi:10.1126/science.aal5166.
[22] Misra RDK, Nune C, Pesacreta TC, Somani MC, Karjalainen LP. Understanding the impact of grain structure in austenitic stainless steel from a nanograined regime to a coarse-grained regime on osteoblast functions using a novel metal deformation–annealing sequence. Acta Biomater 2013;9(4):6245–58. https://doi.org/10.1016/j.actbio.2012.12.003.
[23] Yin F, Xu R, Hu S, Zhao K, Yang S, Kuang S, Li Q, Han Q. Enhanced mechanical and biological performance of an extremely fine nanograined 316 L Stainless steel cell-substrate interface fabricated by ultrasonic shot peening. ACS Biomater Sci Eng 2018. doi:10.1021/acsbiomaterials.8b00173.
[24] Azadmanjiri J, Berndt CC, Kapoor A, Wen C. Development of surface nanocrystallization in alloys by surface mechanical attrition treatment (SMAT). Crit Rev Solid State Mater Sci 2015;40(3):164–81. doi:10.1080/10408436.2014.978446.
[25] Estrin Y, Vinogradov A. Extreme grain refinement by severe plastic deformation: a wealth of challenging science. Acta Mater 2013;61(3):782–817. doi:10.1016/j.actamat.2012.10.038.
[26] Umemoto M. Nanocrystallization of steels by severe plastic deformation. Mater Trans 2003;44(10):1900–11. doi:10.2320/matertrans.44.1900.
[27] Chan HL, Ruan HH, Chen AY, Lu J. Optimization of the strain rate to achieve exceptional mechanical properties of 304 stainless steel using high speed ultrasonic surface mechanical attrition treatment. Acta Mater 2010;58(15):5086–96. doi:10.1016/j.actamat.2010.05.044.
[28] Li N, Li YD, Li YX, Wu YH, Zheng YF, Han Y. Effect of surface mechanical attrition treatment on biodegradable Mg-1Ca alloy. Mater Sci Eng C Mater Biol Appl 2014;35:314–21. doi:10.1016/j.msec.2013.11.010.
[29] Arifvianto B, Suyitno. Surface roughness and wettability of AISI 316 L induced by surface mechanical attrition treatment with different milling ball diameter. In: Proceedings of the international conference on instrumentation, communication, information technology, and biomedical engineering; 2009. p. 1–4. doi:10.1109/ICICI-BME.2009.5417294.
[30] Arifvianto B, Suyitno, Mahardika M. Roughness reduction in AISI 316 L stainless steel after surface mechanical attrition treatment (SMAT). In: Proceedings of the AIP conference proceedings, 1415; 2011. p. 28–31. doi:10.1063/1.3667212.
[31] Arifvianto B, Suyitno, Mahardika M. Effects of surface mechanical attrition treatment (SMAT) on a rough surface of AISI 316 L stainless steel. Appl Surf Sci 2012;258(10):4538–43. https://doi.org/10.1016/j.apsusc.2012.01.021.
[32] Arifvianto B, Suyitno, Mahardika M, Dewo P, Iswanto PT, Salim UA. Effect of surface mechanical attrition treatment (SMAT) on microhardness, surface roughness and wettability of AISI 316 L. Mater Chem Phys 2011;125(3):418–26. doi:10.1016/j.matchemphys.2010.10.038.
[33] Sun Z, Chemkhi M, Kanoute P, Retraint D. Fatigue properties of a biomedical 316 L steel processed by surface mechanical attrition. In: Proceedings of the IOP conference series: materials science and engineering, 63; 2014. 012021. https://iopscience.iop.org/article/10.1088/1757-899X/63/1/012021/meta.
[34] Zhu L, Guan Y, Wang Y, Xie Z, Lin J, Zhai J. Influence of process parameters of ultrasonic shot peening on surface roughness and hydrophilicity of pure titanium. Surf Coat Technol 2017;317:38–53. doi:10.1016/j.surfcoat.2017.03.044.
[35] Zhu L, Guan Y, Wang Y, Xie Z, Lin J. Influence of process parameters of ultrasonic shot peening on surface nanocrystallization and hardness of pure titanium. Int J Adv Manuf Technol 2016;89(5–8):1451–68. doi:10.1007/s00170-016-9181-4.
[36] Huang G-R, Tsai WY, Huang JC, Hu C-K. Analytical modelling for ultrasonic surface mechanical attrition treatment. AIP Adv 2015;5(7):077126. doi:10.1063/1.4926811.
[37] Chaise T, Li J, Nélias D, Kubler R, Taheri S, Douchet G, Robin V, Gilles P. Modelling of multiple impacts for the prediction of distortions and residual stresses induced by ultrasonic shot peening (USP). J Mater Process Technol 2012;212(10):2080–90. doi:10.1016/j.jmatprotec.2012.05.005.
[38] Zhang XC, Lu J, Shi SQ. A computational study of plastic deformation in AISI 304 induced by surface mechanical attrition treatment. Mech Adv Mater Struct 2011;18(8):572–7. doi:10.1080/15376494.2011.621828.
[39] Dai K, Villegas J, Stone Z, Shaw L. Finite element modeling of the surface roughness of 5052 Al alloy subjected to a surface severe plastic deformation process. Acta Mater 2004;52(20):5771–82. doi:10.1016/j.actamat.2004.08.031.
[40] Badreddine J, Micoulaut M, Rouhaud E, Remy S, Retraint D, François M. Effect of the confinement on the properties of ultrasonic vibrated granular gases. Granul Matter 2013;15(3):367–76. doi:10.1007/s10035-013-0397-9.
[41] Badreddine J, Rouhaud E, Micoulaut M, Remy S. Simulation of shot dynamics for ultrasonic shot peening: effects of process parameters. Int J Mech Sci 2014;82:179–90. doi:10.1016/j.ijmecsci.2014.03.006.
[42] Badreddine J, Rouhaud E, Micoulaut M, Retraint D, Remy S, Francois M, Viot P, Doubre-Baboeuf G, Le Saunier D, Desfontaine V. Simulation and experimental approach for shot velocity evaluation in ultrasonic shot peening. Mec Ind 2011;12(3):223–9. doi:10.1051/meca/2011114.
[43] B. Sarabi, Design of ultrasonic shot peening device, in: School of Industrial and Information Engineering, Politecnico Di Milano (Lecco Campus), 2016–2017.
[44] Badreddine J, Remy S, Micoulaut M, Rouhaud E, Desfontaine V, Renaud P. CAD based model of ultrasonic shot peening for complex industrial parts. Adv Eng Softw 2014;76:31–42. doi:10.1016/j.advengsoft.2014.05.010.
[45] Badreddine J, Rouhaud E, Micoulaut M, Remy S, Desfontaine V, Renaud P. 3D Model of shot dynamics for ultrasonic shot peening. Mater Sci Forum 2013;768-769:503–9. doi:10.4028/www.scientific.net/MSF.768-769.503.
[46] Yan Z, Wilkinson SK, Stitt EH, Marigo M. Discrete element modelling (DEM) input parameters: understanding their impact on model predictions using statistical analysis. Comput Part Mech 2015;2(3):283–99. doi:10.1007/s40571-015-0056-5.
[47] Umbrello D, M'Saoubi R, Outeiro JC. The influence of Johnson–Cook material constants on finite element simulation of machining of AISI 316 L steel. Int J Mach Tools Manuf 2007;47(3–4):462–70. doi:10.1016/j.ijmachtools.2006.06.006.
[48] He X, Rong J-L, Xiang D-l. Damage analysis of aluminium foam panel subjected to underwater shock loading. Shock Vib 2017;2017:1–13. doi:10.1155/2017/6031414.
[49] ASM Aerospace Specification Metals Inc. AISI type 304 stainless steel, http://asm.matweb.com/search/SpecificMaterial.asp?bassnum=mq304a; 2017 [accessed 7 June 2017].
[50] AZO MATERIALS. Titanium alloys-Ti6Al4V grade 5, https://www.azom.com/properties.aspx?ArticleID=1547; 2017 [accessed 8 July 2017].
[51] Micoulaut M, Mechkov S, Retraint D, Viot P, François M. Granular gases in mechanical engineering: on the origin of heterogeneous ultrasonic shot peening. Granul Matter 2007;9(1–2):25–33. doi:10.1007/s10035-006-0018-y.

[52] Seifried R, Schiehlen W, Eberhard P. Numerical and experimental evaluation of the coefficient of restitution for repeated impacts. Int J Impact Eng 2005;32(1–4):508–24. doi:10.1016/j.ijimpeng.2005.01.001.
[53] Yin F, Liu YF, Xu R, Zhao KJ, Partin A, Han QY. Nanograined surface fabricated on the pure copper by ultrasonic shot peening and an energy-density based criterion for peening intensity quantification. J Manuf Process 2018;32:656–63. doi:10.1016/j.jmapro.2018.04.003.
[54] J. Cammett, Shot peening coverage–the real deal, in: the shot peener, 2007, pp. 8–14.
[55] Cao SC, Zhang X, Lu J, Wang Y, Shi S-Q, Ritchie RO. Predicting surface deformation during mechanical attrition of metallic alloys. npj Comput Mater 2019;5(1). doi:10.1038/s41524-019-0171-6.
[56] Avrami M. Kinetics of phase change. I general theory. J Chem Phys 1939;7(12):1103–12. doi:10.1063/1.1750380.
[57] Hassani-Gangaraj SM, Moridi A, Guagliano M. From conventional to severe shot peening to generate nanostructured surface layer: a numerical study. IOP Conf Ser Mater Sci Eng 2014;63:012038. doi:10.1088/1757-899x/63/1/012038.
[58] Gangaraj SMH, Guagliano M, Farrahi GH. An approach to relate shot peening finite element simulation to the actual coverage. Surf Coat Technol 2014;243:39–45. doi:10.1016/j.surfcoat.2012.03.057.
[59] Heydari Astaraee A, Miresmaeili R, Bagherifard S, Guagliano M, Aliofkhazraei M. Incorporating the principles of shot peening for a better understanding of surface mechanical attrition treatment (SMAT) by simulations and experiments. Mater Des 2017;116:365–73. doi:10.1016/j.matdes.2016.12.045.